

# Helical Shift Mechanics of Rubber V-Belt Variators

Francesco Sorge, Marco Cammalleri

Dipartimento di Ingegneria Industriale – Università di Palermo

Viale delle Scienze, 90128 – Palermo, Italy

(francesco.sorge@unipa.it / marco.cammalleri@unipa.it)

## Abstract

*A very common configuration of motorcycle V-belt variators allows for the correction of the belt tensioning in dependence on the resistant torque by a suitable helical shape of the tracks that enable the closure/opening of the driven half-pulleys. The theoretical model for the belt-pulley coupling is just complex for this arrangement, where one half-pulley may run in advance and the other is slower than the belt, and requires the repeated numerical solution of a strongly non-linear differential system by a sort of shooting technique, until all boundary conditions are fulfilled (angular contact extent, torque, axial force). After solving the full equations, the present study develops closed-form approximations characterized by an excellent fit with the numerical plots and proposes a simple and practical formulary for the axial thrust in dependence on the torque and the tension level. Then, results of a theoretical-experimental comparison are also reported, revealing a very good agreement of the model with the real operation.*

## List of symbols

$a, b$	regression coefficients of Eq. (11)	$k = 2 \tan \alpha S_t / S_l$	belt stiffness number
$d$	diameter of helical track [mm]	$k_1 = k \tan(\alpha + \arctan f) / \tan \alpha$	
$f, f_s$	sliding and static friction coefficients	$k_2 = k \tan(\alpha - \arctan f) / \tan \alpha$	
$f_a \leq f_s$	adhesion factor	$K$	spring constant of driven actuator [N/mm]
$F_z$	axial thrust [N]	$m, n$	regression parameters for Eq. (11)
$F_{z0}$	spring pre-load on fully closed driven pulley [N]	$m_c$	total centrifugal mass of driver actuator [g]
$\mathbf{F}'_w$	wall force per unit angle [N]	$M$	torque [Nm]
$\mathbf{i}_b$	unit vector parallel to belt	$p = x_{out} / \varepsilon_{d,out}$	penetration-to-elongation asymptotic ratio
		$r$	radius [mm]
		$r_c$	radial coordinate of roller center [mm]

$r_t$	track radius of driven actuator [mm]	$\psi$	belt velocity angle (Fig. 3)
$r_{t0}$	radial coordinate of track center of driver actuator [mm]	$\omega$	angular velocity [ $s^{-1}$ ]
$r_\infty$	wrap radius for infinite transverse stiffness of the belt [mm]	$\Omega = \omega_s / \omega_f$	speed ratio between sliding and fixed half-pulleys
$S_l, S_t$	longitudinal and transverse belt stiffness [N]	<b>Subscripts and superscripts</b>	
$S_f$	flexural belt stiffness [ $Nmm^2$ ]	$b$	parallel to belt
$t$	time [s]	con.	connection point between sub-regions
$T$	belt force [N]	$d$	dynamical belt force, elongation
$u$	dimensionless circumferential component of sliding velocity	$E$	contact exit endpoint
$\mathbf{v}, \mathbf{v}_s$	total and sliding velocities [m/s]	$f$	fixed half-pulley
$x = (r_\infty - r) / r_\infty$	dimensionless belt penetration	in	initial point of main inner region
$z_{t0}$	axial coordinate of track center of driver actuator [mm]	$n$	normal to pulley wall
$\alpha$	groove half-angle	$N$	driven pulley
$\beta_s, \beta_f$	actuator track slopes on driver side	out	final point of main inner region
$\gamma, \gamma_w$	sliding angle (on plane of rotation, on pulley wall)	$p$	peripheral wall force
$\delta$	helical track slope on driven side	$R$	driver pulley
$\varepsilon = T/S_l$	belt longitudinal elongation	$s$	sliding half-pulley
$\theta$	angular coordinate	$S$	slack strand
$\mu$	belt mass per unit length [g/mm]	$T$	tight strand
$\rho = \dot{r} / (\omega_f \cdot r) \cong \dot{r}_\infty / (\omega_f \cdot r_\infty)$	shift-to-peripheral speed ratio	$U$	upstream point of adhesive region
$\chi$	belt penetration angle (Fig. 3)	$w$	pulley wall
		$(\dots)' = \partial(\dots) / \partial\theta$	
		$(\dots)^{\bullet} = \partial(\dots) / \partial t$	

## 1. Introduction

All continuously variable transmissions (CVT) for vehicle application alternate up-shift and down-shift phases of the speed ratio in a typically random manner in order to comply with the driving requests. Besides, due to the relatively low efficiency of the variable speed unit, proper

strategies are requested for reducing or increasing the clamping thrust on the pre-forcing pulley in dependence on the lower or higher resistant torque level. In cases of small power, as for example in motorcycles, a common full-automatic solution consists in controlling the speed ratio by centrifugal masses on the driver side, exerting the closure force through spring loads on the driven side and enslaving the axial push to the resistant torque by proper helical tracks between the driven half-pulleys. The consequence of this kinematical constraint is that the two plates do not rotate synchronously in shift conditions, but the sliding one is in advance or in retard with respect to the other, in the closing or opening period respectively.

While the steady behavior of the belt drives can be considered already established [1-6], only a few theoretical approaches to the shift state may be found in the literature (e. g. see [7-12], also for an overview on other references). Thus, a wide experimental campaign has been carried out by the authors' team on motorcycle variators and attempts at formulating either complete or simplified practical models for design purposes have been carried out. Due to the helical arrangement of the driven half-pulley tracks, the translational closure theory of [7] has been modified in order to consider the different sliding conditions of the belt on the fixed and movable plates. On the contrary, the theoretical approach of [7] remains applicable to the driver pulley and involves the presence of adhesive or adhesive-like sub-regions inside the arc of contact, for the closing or opening phases respectively. Proofs of the existence or non-existence of these sub-regions were given in [7], highlighting their characteristics, which might be referred back, in a remote but strict connection, to the well-known Grashof's concept of adhesive arc (*Ruhebogen*). The one-dimensional thin belt approach has been applied, considering the belt as a continuous material flowing inside a very thin stream tube formed by its own external surface, which is in motion during the shift. Moreover, any micro-tribological aspect of the belt-pulley contact has been disregarded due to the need of limiting the complexity of the whole mathematical model.

Getting numerical solutions is quite laborious for either relative motion of the half-pulleys, axial or helical, and demands much care because of the strong non-linearity of the system equations, of their "boundary layer" nature and of their consequent aptitude to an unstable numerical trend. Actually, the present analysis belongs to the category of "degenerescent" problems, where a small scale factor multiplies one of the highest derivatives, and thus, similarly to other analogous classical problems, such as e. g. the van der Pol relaxation oscillations or the boundary layer flows, the solutions are very sensitive to small changes of the boundary/initial conditions (see [1], Section 4), which sensitivity is additionally worsened by the one-dimensionality. Furthermore, the numerical integration, to be carried out for example by some Runge-Kutta routine starting from one of the two endpoints, must be reiterated by a sort of shooting technique until all the external boundary

conditions are fulfilled (wrap arc, applied torque and axial thrust). Therefore, in addition to the full equation solution, a second important objective of this study is to devise proper closed-form approximate solutions in order to frame a simplified formulary useful for practical purposes, as will be shown in Section 3.

Hence, as such closed-form solutions permit a prompt calculation of the main characteristics of the drive, i. e. the free strand tensions and the axial forces on the two pulleys, a comparison of the theory with several experimental results can be also carried out, as reported in Section 4.

## 2. Comparative Analysis of the Axial and Helical Shift Mechanics

In parallel with the theory of [7], the changes implied by the helical shift motion of the driven pulley plates will be specified in the following. Figures 1-3 describe the scheme of the variable speed drive and show in particular the two actuators, the wall force components acting on an elementary belt segment and a fixed dihedral control volume with the projection on the plane of rotation of the triangles of velocities on the two sides.

The non-dimensional penetration variable  $x = (r_\infty - r) / r_\infty$  is scaled by the nominal radius  $r_\infty$  and, denoting the partial differentiation with respect to  $\theta$  with primes, the geometrical relationship  $r' = -r \tan \chi$  changes into

$$x' = (1-x)\tan \chi \quad \rightarrow \quad x' \cong \tilde{\chi} \quad (1), (1\sim)$$

where the tilde notation (...~) will henceforth indicate the approximate form of the homologous equations (...), neglecting small order terms.

The total time derivative of the radial coordinate of a moving belt element can be written as the sum of a local and a convective term,  $dr/dt = \dot{r} + \dot{\theta} r'$ , where dots indicate partial differentiation with respect to the time  $t$ . Since  $dr/dt = -v \sin \psi$  and  $\dot{\theta} = v \cos \psi / r$ , one has  $v \sin \psi = v \cos \psi \tan \chi - \dot{r}$ .

Distinguishing the sliding and fixed half-pulleys with the subscripts  $s$  and  $f$  respectively, their angular velocities are equal for the driver pulley but are different for the driven pulley, (see Figs. 1 and 3), i. e.  $\omega_s = \omega_f + \Delta\omega = \omega_f + 4\dot{r} \tan \delta \tan \alpha / d = \omega_f (1 + 4\rho \tan \delta \tan \alpha / d)$ , where  $2\dot{r} \tan \alpha$  is the axial velocity of the movable half-pulley,  $\delta$  and  $d/2$  are the helical slope and radius,  $\rho = \dot{r} / (\omega_f \cdot r) \cong \dot{r}_\infty / (\omega_f \cdot r_\infty)$  is the shift-to-peripheral speed ratio, referred to the fixed half-pulley, and one may put  $\delta = \Delta\omega = 0$  for the driver pulley. Notice that  $\Delta\omega$  is positive or negative for the closing or opening phases ( $\rho > 0$  or  $\rho < 0$ ) and is quite small, because  $\rho$  is usually of order 1/1000 or lower, i. e. of the same order of magnitude of the belt elastic deformation.

As a consequence of the different angular speeds of the sliding and fixed plates, two different slip angles must be defined, on the pulley walls,  $\gamma_{w,s}$  and  $\gamma_{w,f}$  (Fig. 2), and on the plane of rotation,  $\gamma_s$  and  $\gamma_f$  (Fig. 3), whence two triangles of velocities can be observed in Fig. 3, which yield the kinematical relationships  $v \cos \psi = \omega_s r + v \sin \psi \tan \gamma_s$  and  $v \cos \psi = \omega_f r + v \sin \psi \tan \gamma_f$ . The above trajectory equation,  $v \sin \psi = v \cos \psi \tan \chi - \dot{r}$ , and the last two kinematical relationships can be combined into

$$\frac{v \cos \psi}{\omega_f \cdot r} = \frac{1 - \rho \tan \gamma_f}{1 - \tan \chi \tan \gamma_f} \quad \frac{1 - \rho \tan \gamma_f}{1 - \tan \chi \tan \gamma_f} = \frac{\Omega - \rho \tan \gamma_s}{1 - \tan \chi \tan \gamma_s} \quad (2a,b)$$

where  $\Omega = \omega_s/\omega_f = 1 + 4r\rho \tan \alpha \tan \delta/d$ . For the driver pulley, one has  $\omega_s = \omega_f = \omega$ ,  $\Omega = 1$ ,  $\gamma_s = \gamma_f = \gamma$ , and observes that, if  $\rho = \tan \chi$  and  $1 - \tan \chi \tan \gamma \neq 0$ , then  $v \cos \psi = \omega r$  and  $v \sin \psi = 0$ , i. e. there is adhesion between the belt and the pulley. Therefore,  $x' = (1 - x)\rho \cong \rho$  along an adhesion sub-region by Eq. (1). In the case of a driven pulley on the contrary, no adhesion sub-region may develop and the relationship between the two sliding angles is obtainable by Eq. (2b)

$$\tan \gamma_s = \frac{1 - \Omega + \tan \gamma_f (\Omega \tan \chi - \rho)}{\tan \chi - \rho} \quad \rightarrow \quad \tan \gamma_s \cong \frac{1 - \Omega + \tan \gamma_f (\Omega \tan \chi - \rho)}{\chi - \rho} \quad (3), (3\sim)$$

Combining the Lagrangian and Eulerian formulations of the mass conservation conditions,  $\mu(1 + \varepsilon) = \text{constant}$  (Lagrange) and  $\partial(\mu r / \cos \chi) / \partial t + \partial(\mu v \cos \psi / \cos \chi) / \partial \theta = 0$  (Euler), where  $\mu$  is the belt mass per unit length,  $\varepsilon = T/S_l \ll 1$  is the longitudinal elongation and  $S_l$  [N] is the longitudinal stiffness, and accounting for Eqs. (1) and (2a), one may arrive, as in [7], at the equation

$$u' = (1 + u) \left[ \frac{\varepsilon'}{1 + \varepsilon} + \tan \chi (1 - \chi') \right] - \rho \quad \rightarrow \quad u' \cong \varepsilon' + \chi - \rho \quad (4), (4\sim)$$

where  $u$  is the dimensionless circumferential component of the sliding velocity on the fixed half-pulley,  $u = v_{s,f} \sin \gamma_f / (\omega_f r) = v \cos \psi / (\omega_f r) - 1 = (\tan \chi - \rho) \tan \gamma_f / (1 - \tan \gamma_f \tan \chi)$ , whence

$$\tan \gamma_f = \frac{u}{(1 + u) \tan \chi - \rho} \quad \rightarrow \quad \tan \gamma_f \cong \frac{u}{\chi - \rho} \quad (5), (5\sim)$$

Neglecting all the inertia terms smaller than the centrifugal forces, which are dominant, the momentum transport theorem can be written in the form  $[(T - \mu v_b^2) \mathbf{i}_b]' + \mathbf{F}'_w \cong 0$ , where  $\mathbf{F}'_w$  is the resultant wall force per unit angle of contact and the term  $\mu v_b^2 \mathbf{i}_b = \mu v^2 \cos^2(\chi - \psi) \mathbf{i}_b$  represents the momentum flux in the belt direction, which however is generally much smaller than  $T$  and may be assumed constant along the belt path. In practice, the belt force  $T$  may be replaced in the analysis by

the "dynamic" force  $T_d = T - \mu v_b^2$  and the "dynamical" elongation  $\varepsilon_d = (T - \mu v_b^2) / S_l$  may be also introduced.

The above equilibrium equation can be split in the directions tangential and normal to the belt on the plane of rotation. Moreover, introducing the belt compression-to-penetration ratio  $2 \tan \alpha$  and the belt transverse stiffness per unit length  $E_z h / w$ , where  $h$  and  $w$  are the belt height and width, the transverse stiffness parameter  $S_t = 2 \tan \alpha E_z h r_\infty^2 / w$  [N] may be defined, which permits expressing the elementary axial push as a function of the radial elastic penetration by means of a transverse "constitutive" equation. Summing up, we have

$$S_l d\varepsilon_d = \sum_{j=f,s} [\sin \alpha \sin \chi + f(\cos \gamma_{w,j} \cos \alpha \sin \chi + \sin \gamma_{w,j} \cos \chi)] dF_{n,j} \quad (6)$$

$$S_l \varepsilon_d (1 + \chi') d\theta = \sum_{j=f,s} [\sin \alpha \cos \chi + f(\cos \gamma_{w,j} \cos \alpha \cos \chi - \sin \gamma_{w,j} \sin \chi)] dF_{n,j} \quad (7)$$

$$dF_z = (\cos \alpha - f \cos \gamma_{w,f} \sin \alpha) dF_{n,f} = (\cos \alpha - f \cos \gamma_{w,s} \sin \alpha) dF_{n,s} = \frac{S_t x(1-x)d\theta}{\cos \chi} \quad (8)$$

Minding that  $\tan \gamma_{w,j} = \cos \alpha \tan \gamma_j$  for  $j = f$  or  $s$ , whence  $\cos \gamma_{w,j} = \text{sgn}(\cos \gamma_j) / \sqrt{1 + \cos^2 \alpha \tan^2 \gamma_j}$   
 $= \cos \gamma_j / \sqrt{1 - \sin^2 \alpha \sin^2 \gamma_j}$  and  $\sin \gamma_{w,j} = \cos \gamma_{w,j} \tan \gamma_j \cos \alpha = \sin \gamma_j \cos \alpha / \sqrt{1 - \sin^2 \alpha \sin^2 \gamma_j}$ ,  
 Equations (8) permit eliminating the elementary wall forces  $dF_{n,j}$  and the wall sliding angles  $\gamma_{w,j}$  from Eqs. (6,7)

$$\varepsilon'_d = \frac{kx(1-x)}{2 \tan \alpha \cos \chi} \sum_{j=f,s} \left[ \frac{\sin \chi \tan \alpha \sqrt{1 - \sin^2 \alpha \sin^2 \gamma_j} + f \sin(\gamma_j + \chi)}{\sqrt{1 - \sin^2 \alpha \sin^2 \gamma_j} - f \tan \alpha \cos \gamma_j} \right] \quad (9)$$

$$\rightarrow \varepsilon'_d \cong \frac{kx}{2 \tan \alpha} \sum_{j=f,s} \left[ \frac{f \sin \gamma_j}{\sqrt{1 - \sin^2 \alpha \sin^2 \gamma_j} - f \tan \alpha \cos \gamma_j} \right] \quad (9\sim)$$

$$\chi' = -1 + \frac{kx(1-x)}{2\varepsilon_d \tan \alpha \cos \chi} \sum_{j=f,s} \left[ \frac{\cos \chi \tan \alpha \sqrt{1 - \sin^2 \alpha \sin^2 \gamma_j} + f \cos(\gamma_j + \chi)}{\sqrt{1 - \sin^2 \alpha \sin^2 \gamma_j} - f \tan \alpha \cos \gamma_j} \right] \quad (10)$$

$$\rightarrow \varepsilon_d \cong \frac{kx}{2 \tan \alpha} \sum_{j=f,s} \left[ \frac{\tan \alpha \sqrt{1 - \sin^2 \alpha \sin^2 \gamma_j} + f \cos \gamma_j}{\sqrt{1 - \sin^2 \alpha \sin^2 \gamma_j} - f \tan \alpha \cos \gamma_j} \right] \quad (10\sim)$$

where the dimensionless stiffness number of the belt,  $k = 2 \tan \alpha S_t / S_l$ , has been introduced as in [2-3]. It is remarkable that Equation (10~) leads to the three notable relationships: 1)  $\varepsilon_d \cong k_1 x$  for  $\gamma_f \cong \gamma_s$

$\cong 0$ , 2)  $\varepsilon_d \cong k_2 x$  for  $\gamma_f \cong \gamma_s \cong \pm\pi$ , 3)  $\varepsilon_d \cong kx$  for  $\gamma_f \cong \gamma_s \cong \pm\pi/2$ , where  $k_1 = k \tan(\alpha + \arctan f) / \tan \alpha$ ,  $k_2 = k \tan(\alpha - \arctan f) / \tan \alpha$  ( $k_2 < 0$  usually).

In conclusion, we have collected four differential equations, Eqs. (1), (4), (9), (10), and two parametric equations, Eqs. (3), (5), in the six variables  $x$ ,  $\varepsilon_d$ ,  $\chi$ ,  $u$ ,  $\gamma_f$  and  $\gamma_s$ , the first four of which are very small (of order  $\sim 1/1000$ ), whilst the sliding angles  $|\gamma|$  may range between 0 and  $\pi$ . For the driver pulley of the CVT under examination, we have one equation less, Eq. (3), and five variables as a whole, because  $\gamma_s = \gamma_f = \gamma$ ,  $\Omega = 1$ .

As specified in [7], the use of the abridged equations (...~) is fairly acceptable in the main internal portion of the arc of contact, but not in the two short boundary regions. Actually, the differential system "degenerates" from the fourth to the third order, when reduced to its abridged form, because Eq. (10) changes into the non-differential relationship (10~) and one of the boundary conditions can no longer be fulfilled. Due to the "boundary layer" type of the problem, the variables are expected to change rather smoothly along most of the arc of contact and exhibit large gradients near the boundaries, in order to fulfill the boundary conditions.

The complete numerical solution has to be calculated as an initial value problem, separately for each pulley, starting from one endpoint of the winding arc, for example the exit point  $E$ , where the transverse compression must be zero ( $x = 0$ ) and proceeding towards the other endpoint, where the variable  $x$  vanishes again. Three initial conditions must be imposed, for  $\varepsilon$ ,  $\chi$ ,  $u$  (or else,  $\gamma_f$  or  $\gamma_s$  in place of  $u$ ), which must be modified by trial and error by a sort of shooting technique until three typical working conditions are fulfilled: contact width  $\Theta$ , traction force  $T_{\text{out}} - T_{\text{in}} = S_l (\varepsilon_{d,\text{out}} - \varepsilon_{d,\text{in}})$  (torque) and axial load  $F_z$ , calculable by Eq. (8)  $F_z = \int_{\text{wrap arc}} S_t x (1-x) d\theta / \cos \chi \cong \int_{\text{wrap arc}} S_t x d\theta$ .

The in-depth analysis of [7] for the axial shifting of the sliding half-pulley (driver side) proves that an internal adhesive region must develop in the closing phase ( $\rho > 0$ ) and an adhesive-like one in the opening phase ( $\rho < 0$ ). In particular, all the previous relationships remain valid in the adhesive sub-region, but considering  $f$  as a variable adhesion factor  $f_a$  and  $\gamma$  as the angle  $\gamma_a$  of the resultant elementary adhesion force in the rotation plane. The adherence limit is reached at the upstream boundary of the adhesive region, where  $f_a = f_s$ ,  $f_s$  being the coefficient of static friction. As  $\tan \chi = \rho = \text{constant}$  and  $u = 0$  along the adhesive region, Equation (4) gives  $\varepsilon' = 0$  (constant belt force), while the integration of Eq. (1) yields, with reference to the upstream endpoint  $U$  of the adhesive region,  $x = 1 - (1 - x_U) \exp[-\rho(\theta - \theta_U)]$ , i. e.  $x \cong x_U + \rho(\theta - \theta_U)$  and  $x' \cong \rho$ . Therefore, the belt path has the shape of a slightly inward coiling logarithmic spiral, which, since  $x$  and  $\rho$  are very small, may be roughly confused with a linear spiral of Archimedes, whose radius increases for fixed  $\theta$  because of the pulley rotation. The axial opening of the driver pulley implies on the contrary

the development of adhesive-like sub-regions with very small sliding velocities, where the dynamical elongation  $\varepsilon_d$  and the elastic penetration  $x$  vary nearly linearly with the angular coordinate, with the gradients  $x' \cong \rho/(1 + k_1)$  and  $\varepsilon'_d \cong k_1\rho/(1 + k_1)$  (see [7], Sect. 4).

Of course, in the helical shift case (driven pulley), the development of an adhesive region must be excluded *a priori*, due to the different velocities of the pulley walls on the two sides of the belt.

By way of example, Figures 4 to 7 report numerical results for the four possible working conditions of a pulley: driver/driven, opening/closing. While the dimensionless shift speed  $\rho$  and the centrifugal force  $\mu v_b^2$  were fixed and the initial values of the variables,  $\varepsilon_{d,E}$  and  $\gamma_{f,E}$  (or simply  $\gamma_E$  for the driver pulley), were imposed at the contact exit point  $E$ , the third initial value  $\chi_E$ , which must be negative because the belt emerges from the groove, was adjusted by an iterative procedure in order to reach a pre-fixed wrap width. In general, it is noteworthy that: 1) a decrease of the exit belt angle  $\chi_E (< 0)$  produces an increase of the contact width, but a great care must be put in avoiding an excessive decrease, which may lead to unacceptable solutions with diverging penetration; 2) small increases of the exit sliding angle  $\gamma_{f,E}$  (or  $\gamma_E$ ), which must be very close to  $\pm\pi$  in order to get acceptable solutions, tend to transform the pulley behavior from driven to idler and then to driver; 3) an increase of the exit elongation  $\varepsilon_{d,E}$  produces an increase of the axial thrust.

The four figures show that the belt angle  $\chi$  is rather small, save in the short seating and unseating regions, where relatively large negative gradients  $\chi'$  are also observable, due to the need of attaining the endpoint condition  $1 + \chi' = 0$  (zero curvature) according with Eq. (10). The sliding angle  $\gamma$  keeps close to 0 and  $\pi$  in such boundary regions, where then the belt tension remain approximately constant, and moreover, while  $\gamma$  shows a smooth connection in the passage from the seating region to the main inner region of contact, it is subject to a sharp variation in the passage from the main region to the unseating region. Therefore, in the search for approximate solutions valid in the main inner region of contact, one may put  $\varepsilon_{d,in} \cong k_1 x_{in}$  at its beginning (subscript  $\dots_{in}$ ), but a similar relationship cannot be written at the end (subscript  $\dots_{out}$ ). Notice that the subscripts ( $\dots_{in}$ ) and ( $\dots_{out}$ ) of the present treatment refer to the endpoints of the main inner region, excluding the small boundary sub-regions of seating and unseating, and do not indicate the whole contact endpoints, where  $x = 0$ .

A new aspect, original with respect to the axial sliding, appears now considering the helical relative sliding. Due to the different angular speeds and the different sliding conditions on the two plates, the whole transmitted torque  $M$  is no longer equally shared between them because the elementary tangential wall forces are not equal and may even have opposite directions in some portion of the arc of contact, as appears on the diagrams of Figs. 6 and 7. The peripheral

components  $F'_p$  of the wall forces per unit angle of contact, on the one and the other plate, can be obtained by Eq. (8), multiplying  $dF_{n,j}$  by  $f \sin \gamma_{w,j}$  and are represented in the figures. For the helical shift, such figures denounce a relevant difference between the two torque fractions, which are proportional to the areas enclosed by the diagrams and the axis  $F'_p = 0$  and may be also negative for the half-pulley with a higher angular speed: the fixed one during the opening phase and the sliding one during the closing phase.

The torque fraction  $M_s/M$  absorbed by the sliding half-pulley depends on the design parameter  $2r_\infty F_z \tan \alpha / M$ , i. e. on the axial-to-traction force ratio  $r_\infty F_z / M$ , on the tension level and on the shift speed. Figure 8 shows the results from the solution of a large number of shift cases and may be used to build practical regression formulas. For  $M \rightarrow \infty$ , the belt-pulley contact tends to the gross slip condition, where  $\gamma_s \cong \gamma_f \cong \pm \pi/2$ ,  $M_s/M \cong 1/2$  and  $M \cong 2f r_\infty F_z / \cos \alpha$ . The starting point on the left of all plots of Fig. 8 has thus the coordinates  $\sin \alpha / f$  and 0.5 and one may try to put  $\ln |(M_s/M) - 0.5| = m \ln |2r_\infty F_z \tan \alpha / M - \sin \alpha / f| + n$ . The first regression constant turns out to be  $m \cong 1.5$  for all diagrams, while the second one,  $n$ , is different for the opening and closing phases. It is found that  $\exp(n)$  is roughly a linear function of the ratio  $\rho / \varepsilon_{\text{out}}$ , whence

$$\frac{M_s}{M} \cong \frac{1}{2} - \left( a \frac{\rho}{\varepsilon_{\text{out}}} + b \right) \left( \frac{2r_\infty F_z \tan \alpha}{M} - \frac{\sin \alpha}{f} \right)^{3/2} \text{sgn}(\rho) \quad (11)$$

where  $a$  and  $b$  are different for the pulley opening and closing ( $\rho < 0$  and  $\rho > 0$ ).

### 3. Analytical Approximations and Design Formulas

As regards the driver pulley, the approximate model is similar to [8], but with the further simplification of prolonging the linear trend of the penetration  $x$  beyond the adhesive/adhesive-like sub-region, to include also the downstream main sliding region. The matching of the analytical curves with the numerical ones remains very good, as shown by the small circles of Figs. 4 and 5.

On the contrary, the helical relative sliding between the driven half-pulleys requires some major changes with respect to [8] and the following model is found to be very suitable for this purpose.

The numerical plots for the driven pulleys indicate that the main inner region of contact may be roughly split into a preceding adhesive-like sub-region and a following main sliding sub-region. In the former sub-region, the value of the penetration angle  $\chi$  is just close to  $\rho$ , although showing a very slightly increasing trend toward upstream. As the plot of the radial penetration  $x$  appears roughly linear, an attempt at a simple approximation for  $x(\theta)$  can be tried putting  $x'(\theta) \cong \text{constant} =$

$3\rho/2$  for the closing phase ( $\rho > 0$ ) and  $x'(\theta) \cong \text{constant} = \rho/2$  for the opening phase ( $\rho < 0$ ). Actually, this assumption yields a fairly good fit with the numerical diagrams in the adhesive-like sub-region, because the shift parameter  $\rho$  is usually quite small and a slight inaccuracy of the model cannot compromise the overall matching with the full solution.

As regards the following main sliding sub-region, the tendency of the sliding angles to become nearly equal on approaching the exit ( $\gamma \cong \gamma_s \cong \gamma_{\text{out}}$ ) is firstly recognizable, as can be also deduced by Eq. (3) observing that  $\tan \gamma$  becomes significantly larger than  $|\rho|$  and  $|1 - \Omega|$ . Moreover, the tendency of the penetration-to-elongation ratio  $x/\varepsilon_d$  and of the gradient ratio  $dx/d\varepsilon_d$  to nearly the same "asymptotic" value is observable:  $dx_{\text{out}}/d\varepsilon_{d,\text{out}} \rightarrow x_{\text{out}}/\varepsilon_{d,\text{out}} \rightarrow \text{constant} = p$ . Then, focusing on the final point of the main sliding region, it is possible to get  $\sqrt{1 - \sin^2 \alpha \sin^2 \gamma_{\text{out}}} = f \cos \gamma_{\text{out}} (kx/\tan \alpha + \varepsilon_d \tan \alpha)/(\varepsilon_d - kx)$  by Eq. (10~), whence, considering that  $0 < \gamma_{\text{out}} < \pi/2$  in the driven case, one obtains as in [3]

$$\tan \gamma_{\text{out}} \cong \frac{\sqrt{(1 - f^2 \tan^2 \alpha)(k_1 p - 1)(1 - k_2 p)}}{\cos \alpha (1 - kp)} \quad (12)$$

Furthermore, replacing the above expression of  $\sqrt{1 - \sin^2 \alpha \sin^2 \gamma_{\text{out}}}$  into Eq. (9~), one gets

$$\varepsilon'_{d,\text{out}} \cong \varepsilon_{d,\text{out}} \cos \alpha \sqrt{(1 - f^2 \tan^2 \alpha)(k_1 p - 1)(1 - k_2 p)} \quad (13)$$

On the other hand, integrating Eq. (4~) from the entrance of the inner region (subscript ...<sub>in</sub>) to a generic  $\theta$ , observing that  $u_{\text{in}}$  is very small, using Eqs. (1~) and (5~) and neglecting small terms, one can obtain  $x' \cong \rho + [\varepsilon_d - \varepsilon_{d,\text{in}} + x - x_{\text{in}} - \rho(\theta - \theta_{\text{in}})]/\tan \gamma$ , where  $x_{\text{in}} = \varepsilon_{d,\text{in}}/k_1$ , as observed in the remarks about Eq. (10~). Using then Eq. (12), one has, at the final point of the main sliding region,

$$x'_{\text{out}} \cong \rho + \varepsilon_{d,\text{out}} \cos \alpha (1 - kp) \frac{1 + p - \frac{\varepsilon_{d,\text{in}}}{\varepsilon_{d,\text{out}}} \left(1 + \frac{1}{k_1}\right) - \frac{\rho}{\varepsilon_{d,\text{out}}} \Theta}{\sqrt{(1 - f^2 \tan^2 \alpha)(k_1 p - 1)(1 - k_2 p)}} \quad (14)$$

where  $\Theta = \theta_{\text{out}} - \theta_{\text{in}}$  is the inner arc width.

Dividing Eq. (14) by Eq. (13), putting  $x'_{\text{out}}/\varepsilon'_{d,\text{out}} = p$ , it is possible to arrive at an algebraic equation for the ratio  $p$ , which can be easily solved in dependence on the physical parameters,  $k, f, \alpha$ , and the drive data,  $T_{\text{in}}, T_{\text{out}}$ :

$$p(1-f^2 \tan^2 \alpha)(k_1 p - 1)(1 - k_2 p) - \frac{\rho}{\varepsilon_{d,\text{out}} \cos \alpha} \sqrt{(1-f^2 \tan^2 \alpha)(k_1 p - 1)(1 - k_2 p)} +$$

$$-(1 - kp) \left[ 1 + p - \frac{\varepsilon_{d,\text{in}}}{\varepsilon_{d,\text{out}}} \left( 1 + \frac{1}{k_1} \right) - \frac{\rho}{\varepsilon_{d,\text{out}}} \Theta \right] = F(p) = 0 \quad (15)$$

The approximate solution for  $x$  can be expressed by a simple parabolic form,  $x = x_{\text{out}} + x'_{\text{out}}(\theta - \theta_{\text{out}}) + x''_{\text{out}}(\theta - \theta_{\text{out}})^2/2$  in the main sliding region, imposing the mentioned final conditions,  $x_{\text{out}} = p\varepsilon_{d,\text{out}}$ ,  $x'_{\text{out}} = p\varepsilon'_{d,\text{out}}$ , and the connection with the upstream adhesive-like solution with the same slope  $x'_{\text{in}} = 0.5\rho [2 + \text{sgn}(\rho)]$ . The second derivative  $x''_{\text{out}}$  and the angular position  $\theta_{\text{con.}}$  of the "connection point" between the two sub-regions, are obtainable by the continuity conditions for  $x$  and  $x'$

$$\theta_{\text{con.}} = \theta_{\text{out}} - 2 \left( \frac{p\varepsilon_{d,\text{out}} - x'_{\text{in}}\Theta - \frac{\varepsilon_{d,\text{in}}}{k_1}}{x'_{\text{out}} - x'_{\text{in}}} \right) \quad x''_{\text{out}} = \frac{x'_{\text{out}} - x'_{\text{in}}}{\theta_{\text{out}} - \theta_{\text{con.}}} \quad (16\text{a,b})$$

The above approximate formulae offer a very fine accordance with the numerical results, as observable by the small circles of Figs. 6 and 7.

The axial thrusts on the driver and driven sides can be easily calculated by the integration of Eq. (8),  $F_z \cong \int_{\text{wrap arc}} S_t x d\theta$ , and, using the subscripts  $R$  and  $N$  for the driver and driven pulleys and the subscripts  $T$  and  $S$  for the tight and slack strands, turn out to be

$$F_{z,R} \cong \frac{(T_T - \mu v_b^2)\Theta_R}{2 \tan(\alpha + \arctan f)} + \frac{\rho_R S_{t,R} \Theta_R^2}{2 + k_{1,R} [1 - \text{sgn}(\rho_R)]} \quad (17)$$

$$F_{z,N} = \frac{(T_S - \mu v_b^2)\Theta_N}{2 \tan(\alpha + \arctan f)} + \frac{x'_{\text{in},N} S_{t,N} \Theta_N^2}{2} + \frac{2S_{t,N}}{3S_l} \left[ \frac{p(T_T - \mu v_b^2) - \frac{T_S - \mu v_b^2}{k_{1,N}} - x'_{\text{in},N} \Theta_N S_l}{p \frac{\varepsilon'_{d,\text{out}}}{\varepsilon_{d,\text{out}}} (T_T - \mu v_b^2) - x'_{\text{in},N} S_l} \right]^2 \quad (18)$$

If the operative data of a V-belt variator are the most usual ones, i. e. transmitted torque, speed and axial thrust on the driven pulley, one has to associate the torque equation

$$T_T - T_S = \frac{1}{2} \left( \frac{M_R}{r_{\infty R}} + \frac{M_N}{r_{\infty N}} \right) \quad (19)$$

with Eq. (18), eliminate one of the two belt forces,  $T_T$  and  $T_S$ , and solve the resulting quadratic equation for the other force. Since what is more significant for the calculation of the axial thrust is

the whole area under the penetration diagram, rather than the local penetration values, the simple model described so far can give a very good accordance with the experimental results, as will be shown in the next section, and appears thus sufficiently reliable.

The overall approximation can be further refined considering the lack of the angle of contact due to the belt arching in the free strands, according to the conventional formula  $\Delta\theta = \left(1/\sqrt{T_T} + 1/\sqrt{T_S}\right)\sqrt{S_f/r_\infty^2}$ , where  $S_f$  is the belt flexural stiffness. Likewise, also the reduction of the axial thrust due to the lower penetration values in the boundary sub-regions could be taken into account as in [5] or [8]. Nevertheless, this axial thrust reduction arises from the hypothesis of a straight configuration of the free strands and of a gradual curvature increase of the belt from the contact boundary points towards the inner arc, and therefore, it is in conflict with the previous belt arching hypothesis, which assumes the curvature  $1/r_\infty$  at the contact endpoints. As a matter of fact, the real free strand condition in a V-belt drive is intermediate between the conventional arching and the straight state, but, since both the effects cut down slightly the full axial thrust, it is roughly legitimate to account for just one of them, e. g. the reduction  $\Delta\theta$ , assuming that it includes the effect of the lower boundary penetration as well.

## 4 Experimentation

Several experimental tests were carried out on a small power rubber belt variator on the test bench of Fig. 9, for various different configurations.

The input power was provided by a DC electric motor, while a pneumatic disk brake exerted the resistant torque. The continuously variable unit was a motorcycle variator and included a downstream reduction gear of ratio  $\cong 13:1$ . The unit was connected to the driving shaft through an upstream gear with a ratio reciprocal of the downstream gearing, with the purpose of limiting the driving motor speed. The stiffness of the various belts used in the tests, in the longitudinal and transverse directions, was measured on a material testing machine for tensile/compression measurements. The coefficient of friction was estimated separately on the driver and driven pulleys, as the plates exhibited different surface finishing. Table 1 reports the data of the characteristic parameters of the CVT.

The speed and torque were measured upstream and downstream of the CVT unit by means of two speed-torque meters of the strain-gauge type and the winding radii on both pulleys were

measured by laser sensors. All electric signals were channeled to a data acquisition system and worked out by a suitable software.

The axial thrust was calculated through an indirect procedure, by the measure of the winding radii and the pre-knowledge of the operative characteristics of the two actuators (see Fig. 1).

On the driver side, a centrifugal mass system with three rollers adjusted the speed ratio to the input speed automatically. The geometrical shape of the roller tracks was detected optically with a great accuracy, as described in ref. [10] and resulted nearly circular in practice. Referring to Fig. 1 and to the list of symbols, using the axial-to-radial displacement ratio  $2\tan\alpha$  (shifting half-pulley vs. belt), one has

$$r_R = r_{R,\min.} + \frac{\Delta z}{2 \tan \alpha}$$

$$(r_{c,\min.} + \Delta r_c - r_{t0})^2 + (\Delta r_c \cot \beta_f - z_{t0} - \Delta z)^2 = r_t^2 \quad (20a,b,c)$$

$$\tan \beta_s = \frac{\Delta r_c \cot \beta_f - z_{t0} - \Delta z}{r_{c,\min.} + \Delta r_c - r_{t0}}$$

and can calculate the roller position  $(\Delta r_c, \Delta z_c)$  and the contact slope  $\beta_s(\Delta r_c)$  in dependence on the belt winding radius  $r_R$ . Then, the roller equilibrium condition yields the axial thrust  $F_{z,R}$ :

$$F_{z,R} \cong \frac{m_c \omega_R^2 (r_{c,\min.} + \Delta r_c)}{\cot \beta_f + \cot \beta_s} \quad (21)$$

On the driver side, the total axial thrust was [10]:

$$F_{z,N} \cong F_{z0} + K(-2\Delta r_N \tan \alpha) + \frac{2M_{N,s}}{d} \tan \delta \quad (22)$$

where  $-2\Delta r_N \tan \alpha (> 0)$  is the spring compression due to the pulley opening and  $M_{N,s}$  the driven torque fraction absorbed by the sliding half-pulley, whose evaluation was done according to Fig. 8, using the mentioned linear regression to correlate the variables.

The upstream and downstream torques losses and the inertia torques were evaluated running each pulley without the belt at constant speed and constant acceleration and were used to correct the externally measured torques in working conditions. Moreover, according to Eq. (19), the torque was averaged between the driver and driven sides in order to consider the belt inelastic stiffness.

The experimental evaluation of the axial forces  $F_{z,R}$  and  $F_{z,N}$  on the belt was done, on the basis of Eqs. (20-22). One of these forces was chosen as an entry for the theoretical model, and to be precise  $F_{z,R}$ , and the calculation of the other axial force ( $F_{z,N}$ ) was carried out by the model for

comparison purposes. In practice, the axial push  $F_{zR}$  was evaluated by Eqs. (20-21), the tight strand tension  $T_T$  by Eq. (17) and then the other tension  $T_S$  by Eq. (19). Then, the torque fraction  $M_{N,s}$  on the driven shifting plate and the experimental axial force  $F_{zN}$  were quickly derived through Eq. (22) and the regression formulas (11), using the following coefficients:  $a_{\text{opening}} = -0.9$ ,  $b_{\text{opening}} = 0.04$ ,  $a_{\text{closing}} = 1.85$ ,  $b_{\text{closing}} = 0.03$ . In parallel, the theoretical value  $F_{zN,\text{theory}}$  was calculated evaluating  $p$  by Eq. (15) and using Eqs. (16) and (18). All this calculation included the reduction of the wrap arc due to the bending stiffness of the belt.

Figures 10 to 13 show the experimental diagrams of the radii, speeds, torques and axial forces during some shift up and shift down phases, together with the tension level on the tight and slack strands and the torque fraction absorbed by the shifting half-pulley on the driven side.

The theoretical axial thrust on the driven side is reported in all figures and a quite fine agreement can be clearly observed between the theory and the experiments. It is noteworthy that this concordance is just acceptable despite the many approximations introduced in the model and the uncertainty of many physical parameters. Furthermore, due to its relative simplicity, the formulary appears quite useful for design purposes when planning the CVT performances.

## 5 Conclusion

The present analysis addresses the mechanical behavior of a very common torque-controlled configuration of rubber V-belt variators, where the relative constraint between the sliding and fixed half-pulleys on the driven side is realized by helical tracks, so that an increase of the resistant torque causes a proportional increase of the axial component of the rail reaction, which in turn strengthens the axial push exerted by a loading spring. The purpose of this device is to save the belt wear and the power losses when the transmission works at partial load and provide the needed tensioning at full load. The mathematical model is different from the axial track case and implies the impossibility of partial sub-regions of contact with adhesive conditions. Moreover, the torque is not equally shared between the two plates, because of the different sliding conditions of the belt on the two side walls, due to the different angular velocities of the half-pulleys.

An in-depth mathematical model has been developed for these torque-controlled variators, considering the elastic penetration of the belt into the groove, consequent to the side compression, and the balance of the mass increase inside a fixed elementary dihedral control volume with the mass flux through its control surface. The system equations are just complex and strongly non-linear, so that their numerical solution is rather troublesome. Running several complete numerical

solutions and observing the diagrams, some easily calculable closed-form approximations can be constructed for the belt radial penetration, which show a fine fit with the full numerical solutions, are applicable to a large variety of different cases and provide a fast tool for the design and the analysis of rubber V-belt drives.

Several shift tests were carried out in different conditions on small rubber belt variators mounted on an experimental bench and measures of the winding radii, torques and speeds on the driver and driven shafts were taken at equally spaced time instants. The instant axial thrust was measured indirectly on each pulley, taking into account the preliminary analysis of the operative characteristics the two actuators, on the driver and driven sides. The driver actuator was of the centrifugal mass type, in order to interlock the motor speed with the speed ratio, while the one on the driven side was of the loading spring type for the belt forcing. The axial thrust values, as calculated by the theory and given by the experiments, were quite comparable, confirming the validity of the theoretical model and the soundness of the closed-form approximations.

## 10 References

- [1] Gerbert, G., 1972, "Force and Slip Behaviour in V-Belt Drives", Acta Polytechnica Scandinavica, No. 67, Helsinki.
- [2] Dolan, J.P., and Worley, W.S., 1985, "Closed-Form Approximations to the Solutions of V-Belt Force and Slip Equations," ASME J. of Mech., Transm. and Autom. in Design, **107**, pp. 292-300.
- [3] Sorge, F., 1996, "A Qualitative-Quantitative Approach to V-Belt Mechanics," ASME J. of Mech. Design, **118**, pp. 15-21.
- [4] Gerbert, G., 1999, Traction Belt Mechanics, Chalmers University of Technology, Göteborg, Sweden.
- [5] Gerbert, G., and Sorge, F., 2002, "Full Sliding "Adhesive-Like" Contact of V-Belts," ASME J. of Mech. Design, **124**, pp. 706-712.
- [6] Kong, L., and Parker, R.G., 2006, "Mechanics and Sliding Friction in Belt Drives with Pulley Grooves," ASME J. of Mech. Design, **128**, pp. 494-502.
- [7] Sorge, F., 2008, "A Theoretical Approach to the Shift Mechanics of Rubber Belt Variators", ASME J. of Mech. Des., (2008), **130**, pp. 122602-(1-9).

- [8] Cammalleri, M., and Sorge, F., "Approximate Closed-Form Solutions for the Shift Mechanics of Rubber Belt Variators", ASME 2009 IDETC/CIE, Aug. 30 - Sept. 2, 2009, San Diego (CA), USA.
- [9] Ide, T., Hirokazu, U., and Kataoka, R., 1996, "Experimental investigation on shift speed characteristics of a metal V-belt CVT", JSAE Paper n. 9636330, CVT '96, Yokohama, Japan.
- [10] Cammalleri, M., 2005, "A new approach to the design of a speed-torque controlled rubber V-belt variator", Proc. of the IMechE, part D, J. of Automobile Engineering, **219**, n. 12, pp. 1413-1428.
- [11] Carbone, G., Mangialardi, L., and Mantriota, G., 2005, "The Influence of Pulley Deformation on the Shifting Mechanism of Metal Belt CVT," ASME J. of Mech. Design, **127**, pp. 103-113.
- [12] Sorge, F., 2007, "Shift Mechanics of Metal Belt CVT," JSAE Paper n. 20074542, CVT Hybrid 2007, Yokohama, Japan.

## Table captions

Table 1. Variator data

## List of figure captions

- Figure 1 a, b Scheme of the actuators on the driver side (a) and driven side (b).
- Figure 2 Interaction between belt and pulley.  
 $C$  = center of belt element,  $AB_fB_s$  = pulley meridian plane,  $CD_sD_f$  = plane of rotation,  $AB_jD_j$  = planes tangent to pulley walls,  $B_jCD_j$  = planes of sliding.
- Figure 3 Control volume. Triangles of velocities.
- Figure 4 Driver solutions during opening phase. Dots: approximate solutions of Section 3.  
Data:  $\alpha = 13^\circ$ ,  $k = 0.115$ ,  $f = 0.4$ ,  $\varepsilon_E = 0.001$ ,  $\mu v_b^2/S_l = 0.0001$ ,  $\rho = -0.0002$   
Entries:  $\gamma_E = -175^\circ$ ,  $\chi_E = -5.1980906^\circ$
- Figure 5 Driver solutions during closing phase. Dots: approximate solutions of Section 3.  
Data:  $\alpha = 13^\circ$ ,  $k = 0.115$ ,  $f = 0.4$ ,  $\varepsilon_E = 0.001$ ,  $\mu v_b^2/S_l = 0.0001$ ,  $\rho = +0.0002$   
Entries:  $\gamma_E = -174^\circ$ ,  $\chi_E = -6.3025879^\circ$
- Figure 6 Driven solutions during opening phase. Dots: approximate solutions of Section 3.  
Data:  $\alpha = 13^\circ$ ,  $k = 0.115$ ,  $f = 0.4$ ,  $\varepsilon_E = 0.001$ ,  $\mu v_b^2/S_l = 0.0001$ ,  $\rho = -0.0002$   
Entries:  $\gamma_{f,E} = -177^\circ$ ,  $\chi_E = -4.9411456^\circ$
- Figure 7 Driven solutions during closing phase. Dots: approximate solutions of Section 3.  
Data:  $\alpha = 13^\circ$ ,  $k = 0.115$ ,  $f = 0.4$ ,  $\varepsilon_E = 0.001$ ,  $\mu v_b^2/S_l = 0.0001$ ,  $\rho = +0.0002$   
Entries:  $\gamma_{f,E} = -176.5^\circ$ ,  $\chi_E = -4.8080541^\circ$
- Figure 8 Driven torque fraction on sliding half-pulley vs. axial-to-traction force ratio, in dependence on the exit elongation and on the shift speed.  
Data:  $\alpha = 13^\circ$ ,  $k = 0.115$ ,  $f = 0.4$ ,  $\mu v_b^2/S_l = 0.0001$
- Figure 9 Experimental test bench
- Figure 10 Test 1. Shift up. Data: see Table 1
- Figure 11 Test 2. Shift up. Data: see Table 1
- Figure 12 Test 3. Shift down. Data: see Table 1
- Figure 13 Test 4. Shift down. Data: see Table 1

belt length	758 mm
centre distance	255 mm
belt width	$w = 16$ mm
unit length mass of belt	$\mu = 0.124$ g/mm
longitudinal stiffness (average)	$S_l \cong 60000$ N
axial stiffness (average)	$S_t \cong 15000$ N
flexural stiffness (average)	$S_f \cong 12500$ N $\times$ mm <sup>2</sup>
groove angle	$\alpha = 13$ deg
belt coefficient of friction on driver pulley	$f_R = 0.37$
belt coefficient of friction on driven pulley	$f_N = 0.4$
total centrifugal mass (primary actuator)	$m_c = 42.6$ g
spring stiffness (secondary actuator)	$K = 4.9$ N/mm
axial pre-load (secondary actuator)	$F_{z0} = 266$ N
angle of helical guides	$\delta = 41$ deg
diameter of helical guides	$d = 40$ mm
variator power	10 kW and over
variator speed	9000 rpm

**Table 1**

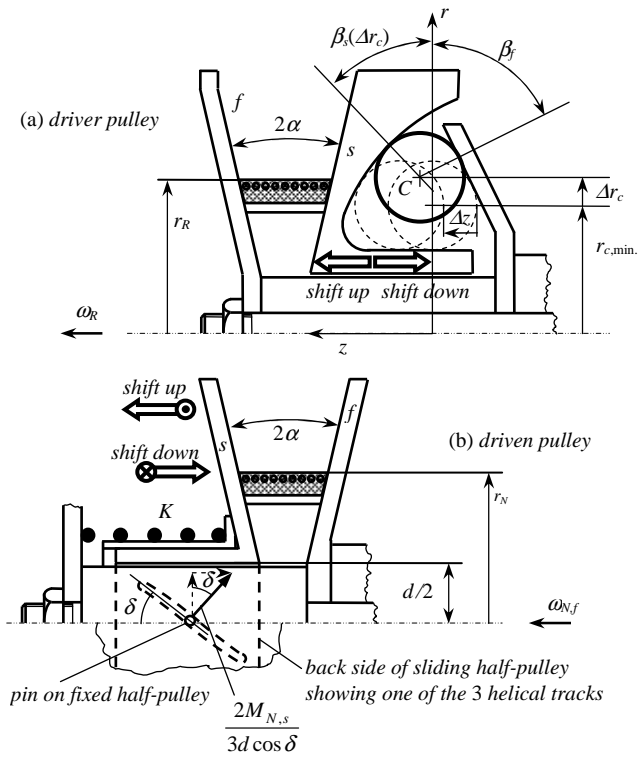


Figure 1 a,b

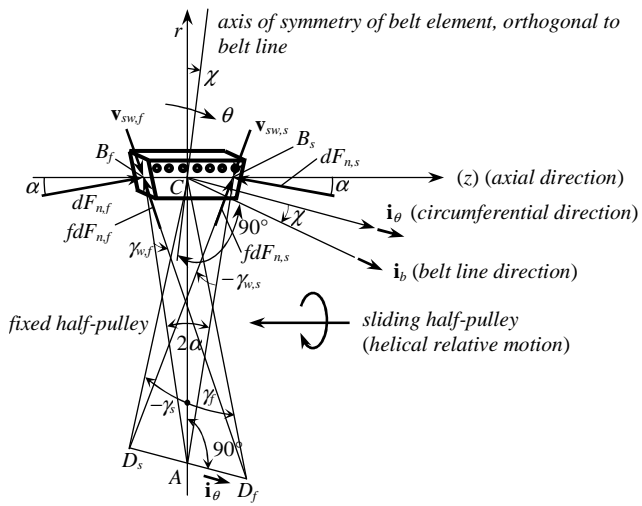


Figure 2

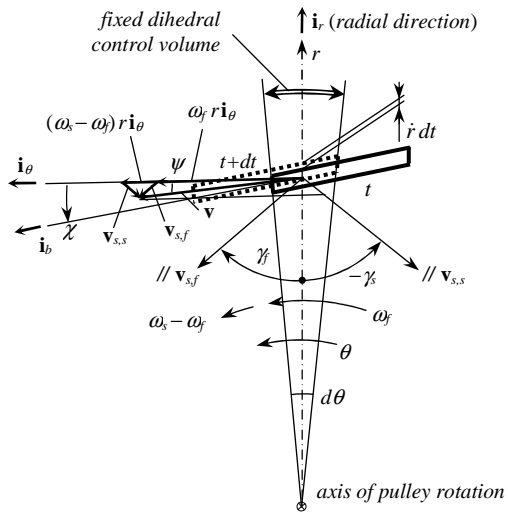


Figure 3

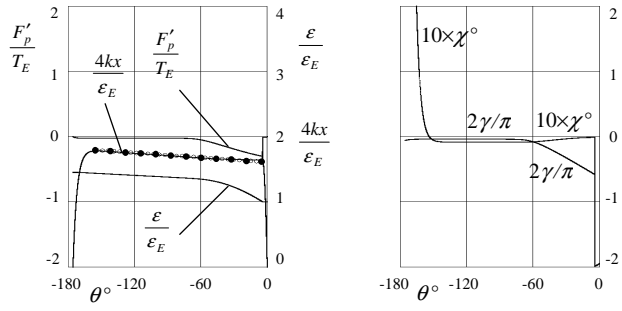


Figure 4

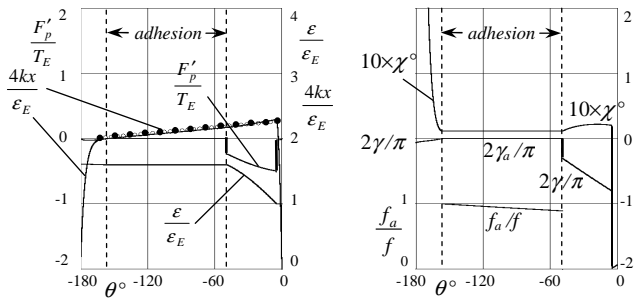


Figure 5

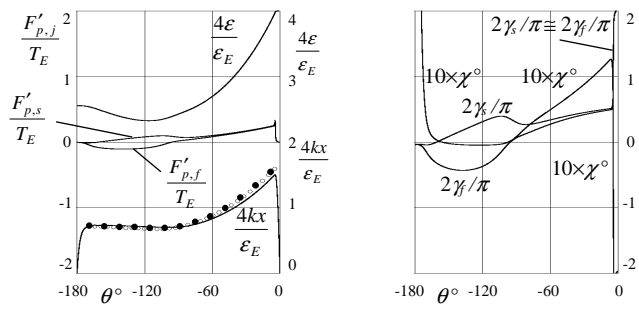


Figure 6

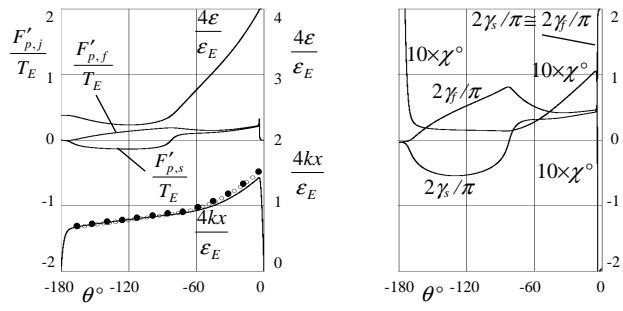


Figure 7

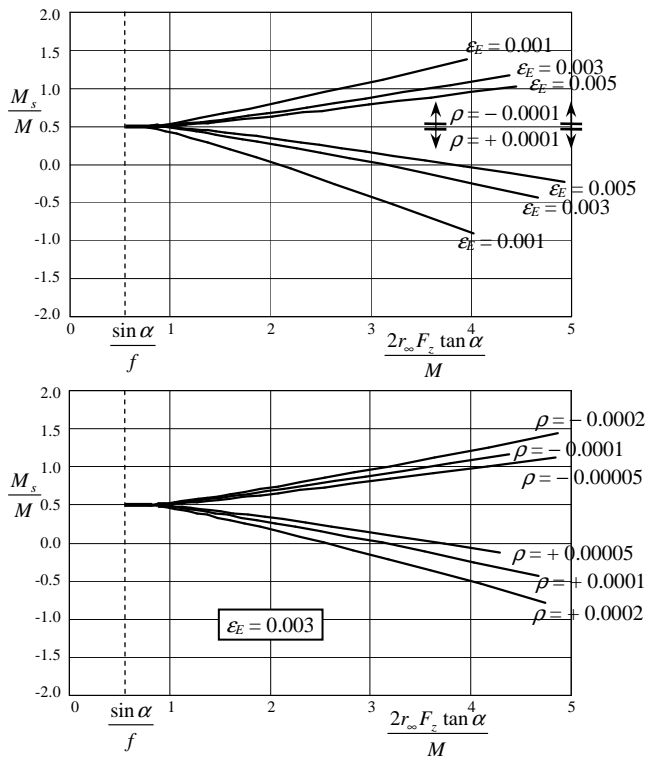
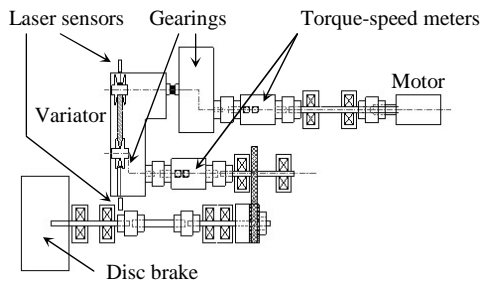


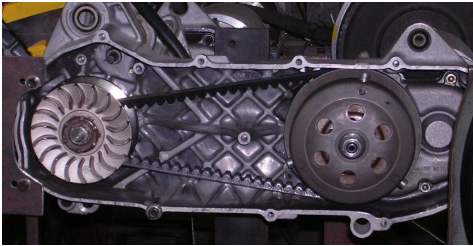
Figure 8



Torque-speed meters



Laser sensor



Variator

**Figure 9**

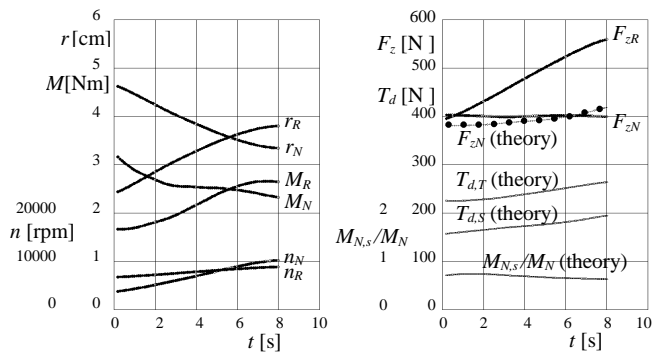


Figure 10

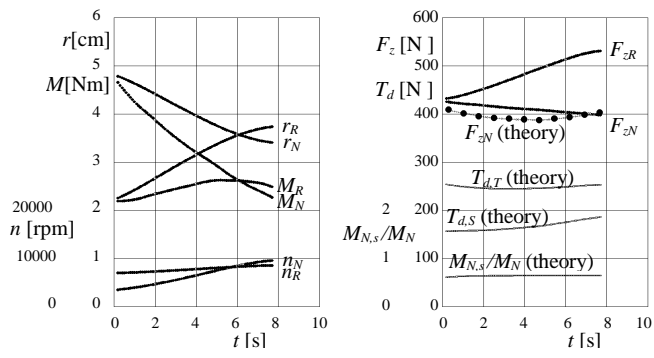


Figure 11

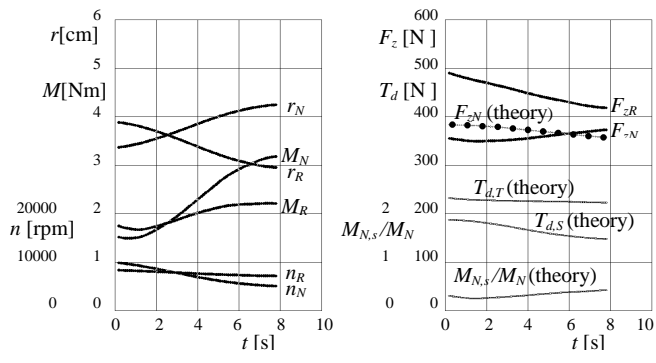


Figure 12

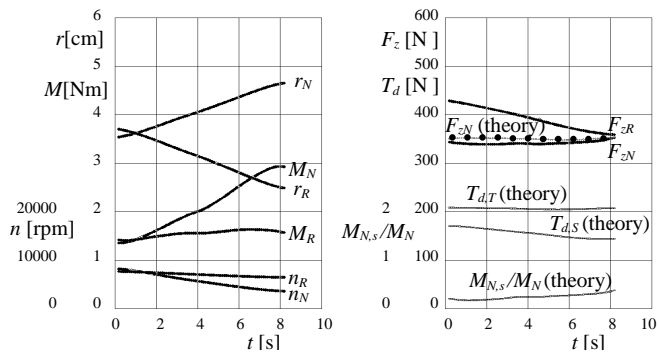


Figure 13